Ping-Pong Modes: A New Form of Multipactor

R. A. Kishek

Institute for Research in Electronics and Applied Physics, University of Maryland, College Park, Maryland 20742, USA

(Received 30 June 2011; published 19 January 2012)

The multipactor is a vacuum discharge based on a secondary electron emission. A novel resonant form is proposed that combines one- and two-surface impacts within a single period, provided the total transit time is an odd number of rf half-periods and the product of secondary yields exceeds unity. For low fD products, the simplest such mode is shown to significantly increase the upper electric field boundary of the multipacting region and lead to overlap of higher-order bands. The results agree nicely with 3D particle-in-cell code simulations. Practical implications of the findings are discussed.

DOI: 10.1103/PhysRevLett.108.035003 PACS numbers: 52.80.Pi, 41.75.−i, 84.40.−x

The multipactor is a vacuum discharge based on a secondary electron emission (SEE) [1]. Often destructive, it can occur in a wide variety of scenarios, such as rf windows [2–4], accelerator structures [5,6], or satellite communication devices [7,8]. A two-surface multipactor in rectangular geometries is generally understood as a resonant discharge, where the electron transit time across the gap has to equal an odd number of rf half-periods. A one-surface multipactor, on the other hand, has been thought to require a dc magnetic or electric field, for example, from the charging of a dielectric surface. Despite discrepancies with experiments and simulations [9], and despite observations of complex electron orbits in computer simulations, theoretical studies of the multipactor remain neatly split into those considering solely a two-surface multipactor and those considering solely a one-surface multipactor. Recent advanced theoretical models such as period-n multipactors [10,11], more complex hybrid resonance modes [9], or a nonresonant "polyphase regime" [12] have remained squarely within the realm of the two-surface multipactor.

In this Letter, I propose a qualitatively different theoretical framework that involves both same-surface and two-surface impacts. The theory developed here successfully and quantitatively agrees with predictions from 3D particle-in-cell code simulations. The new modes are found to significantly extend the region of parameter space for multipactor growth, especially for narrow gaps as found in modern, miniaturized satellite communications devices.

For such gaps, the initial velocity v_0 of the secondaries has been recognized to play an important role in the dynamics [13–15]. Generally, it substantially affects the multipactor boundaries if $N\pi v_0 \sim \omega D$, where $\omega = 2\pi f$ is the rf angular frequency, D the gap separation, and N (odd integer) the order of the multipactor, i.e., the number of half rf periods during the electron transit. Furthermore, a nonzero emission velocity implies that resonance can be maintained for negative emission phases, when the rf electric field is retarding, provided the field changes sign before the electrons impact the originating surface. This concept is used to derive the "cutoff" upper field limit for the multipactor, namely, the maximum electric field for the secondaries to just clear the originating surface.

A multipactor also requires growth, meaning the SEE yield (average number of emitted secondaries for each impacting primary electron) must exceed unity. The majority of the literature implicitly assumes that the yield must exceed unity for *each* impact, but this is not strictly true. Like a period-n multipactor, it is required only that the *product* of the yields over one period exceeds unity. The distinction is poignant considering the higher proportion of backscattered electrons for low primary impact energies [8,16,17].

Hence, we can imagine an entirely new mechanism for the multipactor, illustrated schematically in Fig. 1. For electric fields beyond the cutoff limit, electrons are returned to the surface with a low impact energy. Instead of assuming the discharge is extinguished, as is usually done, we allow the electrons to produce secondaries, reduced in number, which then propagate to the other surface. Below, we derive the fixed points assuming a total transit time of N rf half-periods and demonstrate growth, provided that the product of the yields from the two impacts exceeds unity. Once we permit mixing single-surface and two-surface impacts, we realize the potential for a vast number of mixed modes. We suggest the illustrative term "ping-pong" modes.

To analyze the electron dynamics, we use a 1D parallel-plate geometry with a perpendicular rf electric field

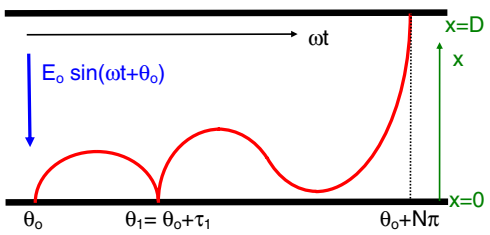

FIG. 1 (color online). Schematic of particle orbits in a period-2 ping-pong multipactor.

(Fig. 1), of the form $E(t) = -E_0 \sin(\omega t + \theta)$, where θ is the rf phase when the electrons enter the gap at $x = 0$. We ignore the effect of the rf magnetic field due to the low energies of the multipacting electrons, which at most can reach a few keV while maintaining an SEE yield greater than unity. An electron (mass m, charge $-e$) will experience an acceleration (nonrelativistic) given by eE/m. In this analysis, it is convenient to use normalized variables: $\tau = \omega t$, $\bar{x} = x/D$, $\bar{v} = v/\omega D$, and $\bar{E}_0 = eE_0/mD\omega^2$, for the time, position, velocity, and electric field, respectively. Using this notation, we integrate the acceleration for an electron launched at $t = 0$ from the plate at $x = 0$ with a fixed, perpendicular velocity component v_0:

$$\bar{v}(\tau, \theta) = -\bar{E}_0[\cos(\tau + \theta) - \cos\theta] + \bar{v}_0, \quad (1)$$

$$\bar{x}(\tau, \theta) = -\bar{E}_0[\sin(\tau + \theta) - \sin\theta - \tau\cos\theta] + \tau\bar{v}_0. \quad (2)$$

For the standard, period-1 (P1), multipactor, the fixed phase θ_0 is obtained by setting $\bar{x}(N\pi, \theta_0) = 1$ in Eq. (2).

The procedure for the period-2 ping-pong (PP2) mode has two steps. First, we solve Eq. (2) with the condition $\bar{x}(\tau_1, \theta_0) = 0$ so as to determine the transit time τ_1 to the first impact as a function of the launch phase. Then, we reapply the equation with the condition $\bar{x}(N\pi - \tau_1, \theta_1) = 1$, where the starting phase is modified to $\theta_1 = \theta_0 + \tau_1$. This results in the following equation pair from which we can determine the unknowns τ_1 and θ_0:

$$0 = -\sin(\theta_0 + \tau_1) + \sin\theta_0 + \tau_1(\cos\theta_0 + u), \quad (3)$$

$$1/\bar{E}_0 = \sin\theta_0 + \sin(\theta_0 + \tau_1) + (N\pi - \tau_1)[\cos(\theta_0 + \tau_1) + u], \quad (4)$$

where $u \equiv \bar{v}_0/\bar{E}_0$. The velocity at each impact can be readily calculated from Eq. (1). It is clear that, for a single-surface multipactor with no dc electric or magnetic fields, the resonance condition $\tau = 2N\pi$ [18] implies no net gain in electron energy above the emission energy, which is generally of the order of a few eV and thus insufficient to cause an avalanche. The PP2 mode breaks the symmetry, permitting a large energy gain during one of the transits.

For theoretical calculations of SEE yield, we use the Vaughan model [19], including dependence of yield on impact angle, but modify it according to Ref. [8] in order to better capture the physics of low-energy primaries. In the simulations described below, we use the code WARP [20], a 3D particle-in-cell code that has been successfully applied to model electron cloud effects in accelerators [21]. WARP uses the POSINST library for modeling SEE [17], which has an extensive description of the SEE parameters including dependence of yield on impact energy and angle, a detailed emission model with angular and energy distributions, and inclusion of backscattered primaries. For the purposes of comparison to simulation, we chose unbaked copper surfaces and selected the parameters of the modified Vaughan model to correspond to the POSINST parameters used by the code. Specifically, we used a peak yield $\delta_{\max} = 2.1$, occurring at an impact energy $W_{\max} = 271$ eV, and a cutoff parameter $W_0 = 6$ eV (see Ref. [8]), resulting in a first crossover point W_1 of 39.4 eV. The yield for impact energies below W_0 is chosen to be 0.7, corresponding to the sum of probabilities of elastic and inelastic backscatter [17]. The theory also assumes monoenergetic emission, with $\frac{1}{2}m{v_{ox}}^2 = \frac{1}{2}m{v_{oy}}^2 = 3$ eV. Here, the normal component v_{ox} is the same as v_0, while the tangential component v_{oy} is unaffected by the rf electric field but is included in the impact angle calculation.

Figure 2 shows the fixed phases from the numerical solution of Eqs. (3) and (4) as a function of $\bar{E}_0$, for $N = 1$ and $\bar{v}_0 = 0.1635$, corresponding to $fD = 1$ GHz mm. The blue solid line indicates the resonant phase for a P1 multipactor. At $\bar{E}_0 \sim 0.5$, the P1 solution becomes unstable and bifurcates into fixed phases of the PP2 mode, illustrated by the black and green solid lines (black for θ_0 and green for $\theta_1 = \theta_0 + \tau_1$). The vertical lines indicate the electric field boundaries for the two regions, with the blue-colored ones corresponding to those for a P1 mode (see [1,13,15]). Note the two upper boundaries: the stability limit (dotted line) and the cutoff limit (dashed line). The low fD products considered here result in reduced impact energies, close to the first crossover point, so the material must be taken into account. The black dotted line indicates a modified lower boundary below which a multipactor can exist from phase considerations, but the energy gain is insufficient. This modified boundary can be calculated from Eq. (1) by setting $\bar{v}(N\pi, \theta_0) = \bar{v}_1 = \sqrt{2W_1/m}/\omega D$.

The multipacting region for the PP2 mode is far wider than that of the P1 mode. The lower PP2 boundary is immaterial, as the multipactor defaults to the P1 mode when the latter is stable [22]. The upper field boundary for the PP2 mode (dashed red line) can be calculated from cutoff considerations in a similar fashion to P1, where the mathematical conditions now become $x(\tau_2, \theta_1) = 0$ and

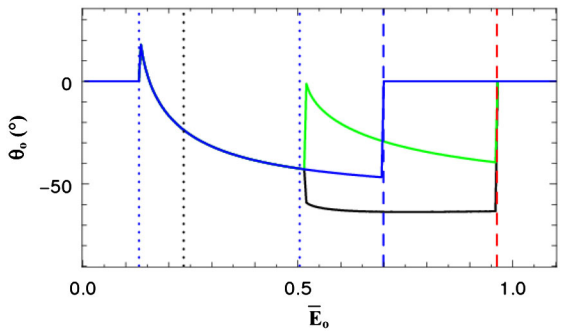

FIG. 2 (color online). Fixed phases as a function of $\bar{E}_0$ for $\bar{v}_0 = 0.149$, for P1 (blue line) and PP2 (black and green lines) modes. The vertical lines are limits from P1 stability (dotted blue line), lower limit due to W_1 (dotted black line), P1 upper cutoff (dashed blue line), and PP2 upper cutoff (dashed red line).

$\bar{v}(\tau_2, \theta_1) = 0$, for $\tau_2 < N\pi - \tau_1$. The stability boundaries of the PP2 mode can be derived from the change of arrival phase after one period due to a departure from the fixed phase at launch. This can be expressed as $|d\theta_2/d\theta_0| < 1$, where

$$\frac{d\theta_2}{d\theta_0} = \frac{\partial\theta_2}{\partial\theta_1}\frac{\partial\theta_1}{\partial\theta_0} = \frac{(N\pi - \tau_1)\sin\theta_1 + u}{\cos\theta_0 + \cos\theta_1 + u} \cdot \frac{\tau_1 \sin\theta_0 + u}{\cos\theta_0 - \cos\theta_1 + u}.$$

The partial derivatives are obtained by implicit differentiation of Eq. (2), evaluated at the limits $\theta = \theta_0$ and θ_1, respectively. In practice, the importance of this limit is doubtful for two reasons. First, a realistic broad distribution of emission velocities [9] tends to make the boundaries more fuzzy. Second, additional focusing is provided by a dynamic mechanism [23] where impacts at phases producing higher yields dominate.

Figure 3 illustrates the growth region by plotting the yield as calculated from the impact velocities. The vertical lines are the same boundaries as in Fig. 2. The dashed lines are the yields calculated from theory: blue for a P1 mode, green for the single-surface impact of the PP2 mode, and black for the two-surface impact, while red is the product of the two PP2 yields. Note that the black and blue dashed lines almost coincide, likely because of the relatively small difference in starting phases and transit times ($\tau_1 \ll 2\pi$). Meanwhile, the single-surface yield is constant at 0.7, which is the value we assumed for impacts below 6 eV, indicating less energetic impacts for all cases in the scan.

To test the theoretical predictions, we set up a 3D simulation model with two parallel plates (0.125 mm thick, 23×23 mm wide) separated by a 2 mm gap. Electrons (5000 particles) are seeded uniformly across the gap, with a thermal velocity distribution, prior to the start of the simulation. We use 640 time steps per rf period (at $f =$ 0.5 GHz), sufficient for accurate trajectories and good diagnostics. The particle weight is held fixed throughout the simulation, so more particles are created if the multipactor is growing. Generally, runs for 5–10 rf periods are sufficient to indicate growth or decay. All the numerical parameters have been thoroughly tested for convergence. Since we are interested in the existence and onset of the multipactor, as opposed to its saturation, the field solver for most simulations is turned off to speed up computations. Test simulations with space charge resulted in similar behavior, apart from wider bunches in phase space, and eventual saturation after the multipactor bunch built to a high density ($\sim 10^8$–10^9 particles). The rf electric field is specified as an external field on a 3D grid and updated every time step. Hence, beam loading effects from the multipactor [1] are ignored, again justified by the focus of this Letter on initiation of the discharge.

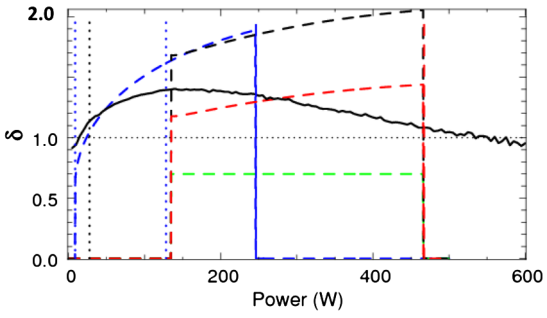

FIG. 3 (color online). SEE yield from P1 (blue line) and PP2 impacts (green and black lines) for unbaked copper. The red curve is the product of the yields from the two ping-pong impacts. The solid black line is the growth rate of the multipactor from WARP simulations as a function of rf power. The vertical lines are the same as in Fig. 2, except the abscissa is transformed to rf power assuming a 50 Ω impedance.

For the first test, we ran a series of 200 simulations scanning the peak electric field over the range $\bar{E}_0 =$ 0–1.1. Assuming the geometry represents the center portion of a waveguide with 50 Ω impedance, this range corresponds to rf powers from 0 to 600 W. The solid black line in Fig. 3 illustrates the average secondary electron yield obtained from the simulations, as a function of rf power. For each simulation, the average yield is calculated by using the formula $(n/n_0)^{1/M}$, where n is the total number of particles at the end of the simulation, n_0 the number of seed particles, and M the number of rf half-periods run. From Fig. 3, it is evident that the multipactor continues to grow for powers far above the stability and cutoff limits predicted for a P1 mode (almost a factor of 4 larger). The point where the secondary yield drops below 1 is close to the cutoff predicted for the PP2 mode. Note the smooth transition from period-1 to the ping-pong mode, likely caused by the spread of electron emission energies and angles in the simulation.

The results presented so far were for a single value of $\bar{v}_0$. We next investigate the dependence of the PP2 mode on this initial velocity or, through the normalization, on fD for a fixed v_0. Figure 4 illustrates the multipactor boundaries from theory for $N = 1$ and $N = 3$. It is clear that the ping-pong mode (red lines) vastly expands the susceptibility region for low fD products. For a P1 multipactor, the $N = 3$ band (dashed blue lines) is narrow and well separated from the $N = 1$ band (solid blue lines). The ping-pong mechanism extends it much further, overlapping with the $N = 1$ band. It seems in fact that the ping-pong mode is the prevalent multipacting mechanism for low fD, given that it occupies a broader region than the "normal" two-surface multipactor. The lower yields associated with the ping-pong mode (evident in Fig. 3) only lengthen the time needed for the discharge to grow to a certain strength.

Figure 5 concentrates on the upper limit of the $N = 1$ band from Fig. 4, comparing it to another series of simulations. Keeping the frequency and the material fixed, the gap separation is adjusted over the range 0.75–15.0 mm so as to vary $\bar{v}_0$. For each gap, we run a series of simulations scanning the electric field strengths, calculate the electron

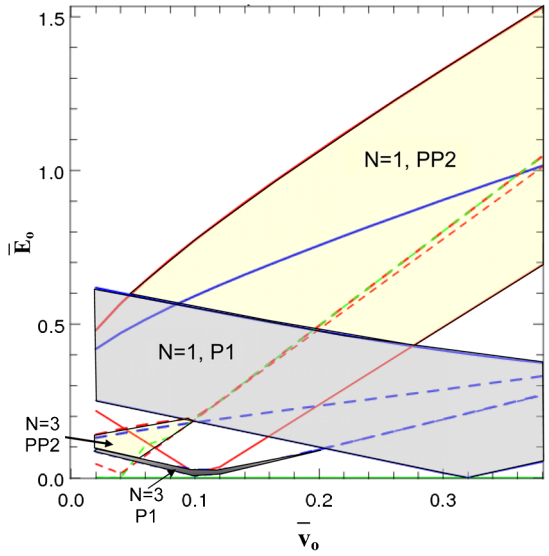

FIG. 4 (color online). Multipactor bounds as function of $\bar{v}_0$ for $N = 1$ (solid line) and $N = 3$ (dashed line). Thin lines correspond to lower limits, while thicker lines correspond to upper limits from cutoff and stability. Both P1 (blue lines and gray-shaded areas) and PP2 (red lines and yellow-shaded areas) regions are shown.

gain from each, and interpolate to find the upper bound. For a fixed material, varying the fD product implies that the average impact energy is reduced for larger $\bar{v}_0$; hence, the yield can drop below unity. The dotted line charts the lower boundary of the P1 multipactor for which the impact energy is W_1. A similar effect is seen on the opposite side, for low $\bar{v}_0$ (high fD), where the energy gain is also reduced as the fixed phase becomes more positive.

These caveats aside, the upper limit obtained from simulation (the circles in Fig. 5) agrees extremely well with the cutoff boundary for the PP2 mode over an intermediate range of $\bar{v}_0$ ($[0.1, 0.2]$ for copper). This has two major implications. First, the ping-pong multipactor is not a mere mathematical construct but can be observed in realistic 3D simulations. Second, this mechanism considerably widens the multipactor susceptibility region by extending the upper field bounds. The concept of "cutoff limit" is muddied by the demonstration of the multipactor's survival despite the return of secondaries to the originating surface.

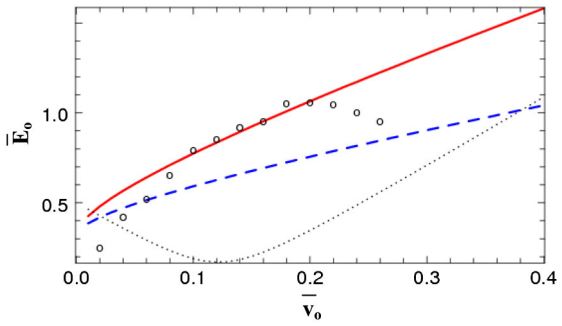

FIG. 5 (color online). The upper cutoff bounds for P1 (blue dashed line) and PP2 (red solid line), compared to WARP simulations (circles). The black dotted line is the lower limit due to W_1 for unbaked copper.

Although we analyzed the simplest such case, involving one single-surface and one two-surface impact per period, we can generalize to a whole class of ping-pong modes, far more mathematically complex to analyze. We can denote them with the notation S^nD^m, where $n, m(>1)$ are the numbers of single- or two-surface impacts per period, respectively. The synchrony condition for these generalized ping-pong modes can be expressed as $\Sigma\tau_k = N\pi$, where the τ_k are the transit times summed over one period and N has the same parity as m.

In this study, we considered copper, which has a modest SEE yield. For dielectrics with high $\delta_{\max}$ and low W_1, one can expect a higher likelihood of ping-pong modes, over a wider range of fD products, including high-period avalanches involving multiple single-surface impacts. The multipactor in dielectrics is important for a class of dielectric-loaded structures being considered for high-gradient acceleration [6]. The cylindrical symmetry of such structures further blurs the line between single-surface and two-surface multipactors, especially when off-normal emission angles are considered. As Sinitsyn, Nusinovich, and Antonsen have shown [24], the particle orbits can be complex and involve several bounces in the same localized part of the waveguide before shooting across the gap. It is interesting to note that Wu and Ang [25] had hinted at the possibility of mixed one- and two-surface modes but ignored it due to their sole focus on the single-surface multipactor. I believe that the ping-pong modes described here are an important step towards a comprehensive theoretical model for multipactor in cylindrical dielectric-loaded structures.

I thank J.-L. Vay and D. P. Grote for their outstanding support of the WARP code and development of the SEE module. I am also grateful for motivating and inspiring discussions with A. Smirnov, A. Murokh, D. Stratakis, G. Nusinovich, I. Haber, and O. Sinitsyn. This work is funded by the U.S. Department of Energy, Office of High Energy Physics.

[1] R. A. Kishek *et al.*, Phys. Plasmas **5**, 2120 (1998), and references therein.
[2] R. A. Kishek and Y. Y. Lau, Phys. Rev. Lett. **80**, 193 (1998).
[3] L. K. Ang, Y. Y. Lau, R. A. Kishek, and R. M. Gilgenbach, IEEE Trans. Plasma Sci. **26**, 290 (1998).
[4] H. C. Kim and J. P. Verboncoeur, Phys. Plasmas **12**, 123504 (2005).
[5] G. Rumolo and F. Zimmermann, Phys. Rev. ST Accel. Beams **5**, 121002 (2002).
[6] J. G. Power *et al.*, Phys. Rev. Lett. **92**, 164801 (2004).

[7] A. D. Wood and J. Petit, Microwave J. **35**, 142 (1992).
[8] C. Vicente *et al.*, in *Proceedings of the 2006 Power Modulator Symposium* (IEEE, New York, 2006), ISSN 1930-885X, pp. 22–27.
[9] A. Kryazhev *et al.*, Phys. Plasmas **9**, 4736 (2002).
[10] A. L. Gilardini, J. Appl. Phys. **71**, 4629 (1992).
[11] S. Riyopoulos, Phys. Plasmas **14**, 112101 (2007).
[12] I. A. Kossyi *et al.*, J. Phys. D **41**, 065203 (2008).
[13] V. D. Shemelin, Sov. Phys. Tech. Phys. **31**, 1029 (1986).
[14] R. A. Kishek, Ph.D. dissertation, University of Michigan, Ann Arbor, 1997.
[15] S. Riyopoulos, Phys. Plasmas **5**, 305 (1998).
[16] V. E. Semenov *et al.*, IEEE Trans. Plasma Sci. **37**, 1774 (2009).
[17] M. A. Furman and M. T. F. Pivi, Phys. Rev. ST Accel. Beams **5**, 124404 (2002).
[18] J. R. M. Vaughan, IEEE Trans. Electron Devices **35**, 1172 (1988).
[19] J. R. M. Vaughan, IEEE Trans. Electron Devices **36**, 1963 (1989).
[20] D. P. Grote, A. Friedman, and I. Haber, Fusion Eng. Des. **32–33**, 193 (1996); J.-L. Vay, Phys. Rev. Lett. **98**, 130405 (2007).
[21] R. H. Cohen *et al.*, Phys. Plasmas **12**, 056708 (2005).
[22] In other words, if multiple stable solutions with different periodicities coexist, we expect that electrons will get trapped in the stable fixed phase of the mode with the lowest number of impacts.
[23] R. A. Kishek and Y. Y. Lau, Phys. Plasmas **3**, 1481 (1996).
[24] O. V. Sinitsyn, G. S. Nusinovich, and T. M. Antonsen, Phys. Plasmas **16**, 073102 (2009).
[25] L. Wu and L. K. Ang, Phys. Plasmas **14**, 013105 (2007).